

Distribution of broad plasma depletions in the equatorial F region observed by the C/NOFS satellite

Jong-Min Choi¹, Young-Sil Kwak², Hyosub Kil³, Jaeheung Park², Woo Kyoung Lee², Yong Ha Kim⁴, and Junseok Hong⁴

¹National Cheng Kung University

²Korea Astronomy and Space Science Institute

³Johns Hopkins University Applied Physics Laboratory

⁴Chungnam National University

November 21, 2022

Abstract

Broad plasma depletions (BPDs) are bubble-like plasma depletions in the equatorial F region whose longitudinal widths (> 4 degree) are greater than those of regular bubbles. Their occurrence in satellite observations is understood in terms of the uplift of the ionosphere; BPDs are observed when satellites pass through the bottomside of bubbles. However, a merger of bubbles is also suggested as the cause of BPDs. We investigate the origin of BPDs by examining the occurrence climatology of BPDs and its association with vertical plasma motion. Our preliminary results derived from the C/NOFS observations in 2008–2012 show that BPDs occur more frequently during lower solar activity, during higher magnetic activity, and at lower altitudes. BPDs during solar maximum and minimum periods show different behavior. BPDs during solar maximum period occur frequently at premidnight and during the equinoxes and December solstices (for highly geomagnetically disturbed periods). On the contrary, BPDs during the solar minimum period occur predominantly at postmidnight and during the June solstices. The occurrence rates of postmidnight BPDs are positively correlated with AE index and are inversely correlated with 10.7 cm solar radio flux. Low solar activity creates favorable conditions for generating BPDs by thinning the F region. At the solar minimum, the density of the F region's bottomside changes significantly even with slight altitude shifts, which can be recognized as BPDs. When a geomagnetic disturbance occurs, the eastward electric field can be enhanced at the equatorial F region, and the entire F layer can move upward.

1 **Distribution of broad plasma depletions in the equatorial F region observed by the**
2 **C/NOFS satellite**

3

4 Jong-Min Choi^{1,2}, Young-Sil Kwak^{2,3*}, Hyosub Kil⁴, Jaeheung Park^{2,3}, Woo Kyoung Lee²,
5 Yong-Ha Kim⁵, and Junseok Hong^{2,5}

6

7 ¹Department of Earth Sciences, National Cheng Kung University, Tainan, Taiwan

8 ²Space Science Division, Korea Astronomy and Space Science Institute, Daejeon, South Korea

9 ³Department of Astronomy and Space Science, Korea University of Science and Technology,
10 Daejeon, South Korea

11 ⁴The Johns Hopkins University Applied Physics Laboratory, Laurel, Maryland, USA

12 ⁵Department of Astronomy and Space Science, Chungnam National University, Daejeon, South
13 Korea

14 -----

15 (*) Corresponding author: Young-Sil Kwak (e-mail: yskwak@kasi.re.kr)

16 Short title: DISTRIBUTION OF BROAD PLASMA DEPLETIONS

17

18 Three main points:

- 19 1. BPDs occur predominantly at postmidnight in comparison to premidnight.
- 20 2. BPDs occur more frequently during periods of low solar activity and during the June
21 solstices.
- 22 3. Generation of BPDs is associated with lower scale height, stagnant background plasma
23 and storm-time disturbance dynamo.

24 **Abstract**

25 Broad plasma depletions (BPDs) are bubble-like plasma depletions in the equatorial F region
26 whose longitudinal widths (> 4 degree) are greater than those of regular bubbles. Their
27 occurrence in satellite observations is understood in terms of the uplift of the ionosphere; BPDs
28 are observed when satellites pass through the bottomside of bubbles. However, a merger of
29 bubbles is also suggested as the cause of BPDs. We investigate the origin of BPDs by examining
30 the occurrence climatology of BPDs and its association with vertical plasma motion. Our
31 preliminary results derived from the C/NOFS observations in 2008–2012 show that BPDs occur
32 more frequently during lower solar activity, during higher magnetic activity, and at lower
33 altitudes. BPDs during solar maximum and minimum periods show different behavior. BPDs
34 during solar maximum period occur frequently at premidnight and during the equinoxes and
35 December solstices (for highly geomagnetically disturbed periods). On the contrary, BPDs
36 during the solar minimum period occur predominantly at postmidnight and during the June
37 solstices. The occurrence rates of postmidnight BPDs are positively correlated with AE index
38 and are inversely correlated with 10.7 cm solar radio flux. Low solar activity creates favorable
39 conditions for generating BPDs by thinning the F region. At the solar minimum, the density of
40 the F region's bottomside changes significantly even with slight altitude shifts, which can be
41 recognized as BPDs. When a geomagnetic disturbance occurs, the eastward electric field can be
42 enhanced at the equatorial F region, and the entire F layer can move upward.

43

44 **1. Introduction**

45 The plasma depletions in the equatorial F region have various sizes of irregularities during
46 the nighttime. A typical phenomenon of irregularities, bubbles, has formation of deep plasma
47 density depletion structures over a narrow longitude and latitude. Sometimes, especially when
48 there is a geomagnetic disturbance, plasma depletion is formed over a wider space, which is
49 called a broad plasma depletion (BPDs). BPDs in the equatorial F region are plasma depletions
50 over several hundred kilometers in longitude and latitude.

51 BPDs were mainly found from in-situ satellite observations during geomagnetic disturbance:
52 the Defense Meteorological Satellite Program (DMSP) at 840 km altitude (Basu et al., 2007;
53 Burke et al., 2000; Greenspan et al., 1991; Kil & Paxton, 2006; Kil et al., 2006), the first
54 Republic of China Satellite (ROCSAT-1) at 600 km altitude (Su et al., 2002), the Korea
55 Multipurpose Satellite-1 (KOMPSAT-1) at 685 km altitude (Lee et al., 2002), and the
56 Communication/Navigation Outage Forecasting System (C/NOFS) from 400 km to 850 km
57 altitude (Burke et al., 2009; Huang et al., 2009; Huang et al., 2011, 2012; Kil & Lee, 2013; Kil et
58 al., 2014, 2016; Lee et al., 2014).

59 There are two hypotheses regarding the mechanism of BPDs; merging bubbles and
60 ionospheric uplift. Merging process is responsible for the BPDs observed near plasma bubbles.
61 Plasma bubbles grow and merge to form BPDs (Huang et al., 2011, 2012; Kil & Paxton, 2006;
62 Kil et al., 2006). However, some BPDs are observed without any signature of plasma bubbles
63 (Kil & Lee, 2013, Kil et al., 2014, 2016; Lee et al., 2014). In other words, BPDs are found in
64 longitudinal regions where C/NOFS did not detect bubbles before BPDs detection. As such, Kil
65 et al. (2013) claimed that bubbles are not a necessary condition for BPDs formation.

66 According to the second hypothesis, the cause of BPDs is a geomagnetic disturbance, which

67 introduces an electric field to the low-latitude ionosphere. The enhanced eastward electric field
68 moves the plasma upward via the $E \times B$ drift. BPDs are detected when the satellites pass through
69 the upwelling edge at F region bottomside during geomagnetic disturbance time. Therefore, a
70 large and wide density depletion has been observed as the satellite observes the region.

71 The goal of this study is to identify the characteristics of BPD occurrence rate and to check
72 the mechanism of BPD generation. For this purpose, we use the measurements of the plasma
73 density taken by the Planar Langmuir Probe (PLP) on board the C/NOFS satellite. The C/NOFS
74 satellite was launched in April 2008 into an elliptical orbit at an altitude of 400 km-850 km. Its
75 orbital inclination was 13° .

76 Though a number of studies have investigated the characteristics of BPDs extensively, there
77 is still room for further improvement. Since DMSP and KOMPSAT-1 are on sun-synchronous
78 orbits, the ionosphere can only be monitored at a limited range of local time. The ROCSAT-1
79 has a circular orbit, and its altitude was fixed at 600 km. The operating period of KOMPSAT-1
80 and ROCSAT-1 is near the peak of solar activity. On the other hand, since C/NOFS has an
81 elliptical orbit, the equator can be observed at various local time regions. In addition, since the
82 altitude orbit is 400 km to 850 km and operating period is from solar minimum to moderate
83 period, the BPD characteristics can be analyzed at various altitudes and solar activities.

84 Furthermore, most of the previous studies have explained the phenomenon with a few
85 examples. We went one step further to find the BPDs automatically and checked their statistical
86 characteristics. The data and methodology are explained in section 2. The results from statistical
87 analysis of the BPDs are shown in section 3. In section 4, we discuss why the rate of BPDs
88 occurrence is high under certain conditions. A conclusion for this study is given in section 5.

89

90 2. Data and methodology

91 The C/NOFS satellite was in an elliptical orbit (altitude: 400 km-850 km) with an orbital
92 inclination of 13 degrees and launched on 16 April 2008. The low-inclination orbit assists in
93 monitoring the ionosphere at all local time sectors. PLP on board the C/NOFS satellite detected
94 the plasma density and temperature in situ. The data sampling rate of PLP is 512 Hz, and allows
95 for detection of irregularities as small as 13 m. In this study, we analyze the plasma density
96 measurements using 1s average data, because the BPDs structure forms over several hundred
97 kilometers.

98 To illustrate the methodology used to automatically detect BPDs, we used BPDs observed
99 on 11 December 2010 as an example. The black curve in Figure 1a shows in situ measurements
100 of the plasma density obtained from the PLP data. The red curve indicates the background
101 density. The background density is determined by repeated smoothing and removal of the low
102 density region. The observed density was smoothed using 50 data points. Then, the background
103 density is obtained by repeating the smoothing operation 5 times based on the assumption that
104 the variation of background density is smooth with respect to longitude.

105 Figure 1b represents the difference between the logarithm of the plasma density (N_i) and
106 logarithm of the background density (N_0). Figure 1c shows the absolute values of the results in
107 Figure 1b. The red dashed line in Figure 1c is the threshold value ($\sigma > 0.2\%$), which is used to
108 remove very small density perturbations. The equatorial ionization trough, which shows a
109 gradual density variation, is not included. The data points exceeding the threshold value in
110 Figure 1c are given as Flag 1, and those that do not exceed the threshold value are treated as Flag
111 0, and the result is shown in Figure 1d. Since we focus on irregularities over several hundred
112 kilometers in longitude and latitude, we have assumed that values above the threshold must be

113 maintained over at least 60 consecutive data points (4 degrees) for longitude. The BPDs based on
114 that assumption are shown in Figure 1e.

115

116 **3. Results**

117 Figure 2a shows the local time distribution of the occurrence of BPDs during 2008-2012.
118 After the BPDs were automatically detected, various parameters corresponding to the median UT
119 values of each of the BPDs were used for statistical analysis. BPDs are detected automatically
120 from the PLP data orbit according to orbit. We processed the PLP data from 2008-2012. The
121 total number of BPDs is 378. There are 53 premidnight BPD events and 325 postmidnight BPD
122 events.

123 BPDs are observed after 18:00 LT and have a peak occurrence rate between 02:00 and
124 04:00 LT. Although BPDs were found at premidnight in previous case studies, our statistical
125 analysis shows that BPDs occur predominantly postmidnight. A number of researchers have used
126 DMSP and KOMPSAT-1 satellite data to study BPDs occurring before midnight due to the Sun-
127 synchronous satellite orbit (Basu et al., 2007; Burke et al., 2000; Greenspan et al., 1991; Kil &
128 Paxton, 2006; Kil et al., 2006, Lee et al., 2002). In ROCSAT-1 and C/NOFS satellite data, BPDs
129 are also observed after midnight (Burke et al., 2009; Huang et al., 2009; Huang et al., 2011, 2012;
130 Kil & Lee, 2013; Kil et al., 2014, 2016; Lee et al., 2002; Lee et al., 2014, Su et al., 2002). In the
131 following discussions, we categorize BPDs into two groups separated by the local midnight,
132 because we can identify different mechanisms depending on the local time.

133 Figure 2b shows the magnetic latitude distribution of BPDs occurrence. BPDs are frequently
134 observed around the magnetic equator within $\pm 5^\circ$ magnetic latitude, regardless of the
135 classification of pre-/post-midnight BPDs. These results indicate that BPDs are not a

136 phenomenon that occur at other latitudes, but near the magnetic equator.

137 Figure 2c shows the occurrence rate of BPDs as a function of K_p . The occurrence rates were
138 presented in the form of a percentage (%) with respect to the total data points during 2008-2012.
139 C/NOFS PLP data are not distributed equally for different K_p values. Therefore, the actual
140 number of BPD occurrences can be biased by the uneven data distribution. As such, the
141 occurrence rate is considered to identify the distribution as function of K_p . The occurrence rates
142 of BPDs show an increasing trend with an increase of K_p . Although the number of premidnight
143 BPDs is very small compared to postmidnight, premidnight BPDs appear primarily in K_p
144 between 6 and 7. This means that premidnight BPDs mainly occur when there is a strong
145 geomagnetic disturbance.

146 BPDs are mostly observed at lower apex altitudes in Figure 2d. According to the BPD
147 formation mechanism suggested by Kil et al. (2014), more BPDs are expected on the F region
148 bottomside because BPDs are nothing but the uplifted bottomside of the F region. This
149 phenomenon can be confirmed in the high-resolution plasma bubble model of Yokoyama et al.
150 (2014), where the F region bottomside bubble more closely resembles BPDs than the F region
151 topside bubble. On the contrary, according to the merging bubble mechanism identified by
152 Huang et al. (2011), more BPDs must be observed at the topside, because the bubble grows
153 vertically and then merges. Therefore, our Figure 2d seems to support Kil et al. (2014), who
154 interpreted BPDs as updraft of F region bottomside.

155 Figure 3 shows the monthly distribution of the occurrence rate of BPDs for five years. BPD
156 occurrences clearly peak at solar minimum. Significantly, most of them are observed in June,
157 while the secondary occurrence maximum occurs in December. According to the uplift
158 mechanism (Kil & Lee, 2013; Kil et al., 2014, 2016; Lee et al., 2014), when the entire F region is

159 lifted up and the satellite passes below it, it is considered as a BPD. Nishioka et al. (2012) also
160 presented that the post-midnight field-aligned irregularities by 30.8 MHz radar and the uplift of
161 the F layer represented by hmF2 were frequently seen around midnight during a solar minimum
162 period between May and August at Kototabang, Indonesia. Figure 3 indicates that the increasing
163 10.7 cm solar radio flux decreases the occurrence of BPDs. When a large number of BPDs are
164 observed, the AE index is relatively high. This is consistent with the explanation that the
165 eastward electric field caused by the geomagnetic activity increases in the equatorial F region
166 around BPDs.

167 In Figure 4, the distributions of the rate of occurrence of BPDs are shown for three seasons:
168 June solstice (May, June, July, and August), December solstice (November, December, January,
169 and February), and Equinox (March, April, September, and October). Then, BPDs are divided
170 into two groups based on the local time. The green curves represent premidnight BPDs, while
171 blue curves indicate postmidnight ones. The 10.7 cm solar radio flux during 2008-2012 is shown
172 with red curves. The rate of occurrence of BPDs tends to decrease with increasing solar activity.
173 BPDs occur more frequently during the period of low solar activity and during the June solstices.
174 This tendency is most prominent in postmidnight BPDs. Seasonally, the negative correlation
175 with solar activity is clearly visible around the June solstice. On the other hand, in December and
176 equinox, the correlation seems weak, albeit certainly negative.

177

178 **4. Discussion**

179 **4.1. Postmidnight BPDs during low solar activity**

180 In this paper, we report the characteristics of the apex height, K_p index, day of year,
181 seasonal and solar activity effects on the equatorial BPDs. Based on the occurrence climatology,

182 BPDs observed by C/NOFS can be characterized as the phenomena at postmidnight, near the
183 magnetic equator, at the lower part of the ionospheric F-region, during solar minimum, and
184 during the June solstice. In particular, postmidnight BPDs are strongly dependent on the solar
185 activity (i.e., occurrence rate of postmidnight BPDs is higher for low solar activity) and occur
186 frequently in June solstice. This solar activity dependence of BPDs occurrence can be related to
187 scale height variations in the ionosphere.

188 In a plasma moving in the vertical direction, the plasma density changes according to the
189 ionospheric thickness, and the change can be expressed by the scale height. The variation of
190 ionospheric electron density at two altitudes (Δn_e) is associated with the height variation (Δh) in
191 the F region bottomside and scale height (H_m) [Hargreaves, 1992].

192

$$\Delta n_e \propto \exp\left(\frac{\Delta h}{H_m}\right)$$

193

194 H_m is a variable influenced by local time, season, and longitude. A low scale height means that
195 density difference between the two altitudes is large – that is, the F region has contracted in its
196 vertical extent. Δh , change of observation altitudes with respect to the F-region peak, is a
197 variable that can be affected by the geomagnetic disturbance. In the equatorial ionosphere, Δh is
198 known to change due to the disturbance-induced electric field.

199 The scale height is known to be related to the bottomside profile thickness. Lee & Reinisch
200 (2007) investigated the scale height near the F region peak measured by digisonde at Jicamarca
201 Radio Observatory (JRO) (11.95°S, 76.87°W) in Peru. Bottomside profile thickness is highly
202 correlated with F₂ layer Chapman scale height (H_m). Liu et al. (2012) reported the variation of

203 thickness measured by Jicamarca digisonde during the last two solar minima: 1996-1997 and
204 2008-2009. At the geomagnetic equatorial station at Jicamarca, the thickness is lowest in June
205 solstice 2008-2009, with very low solar activity. Liu et al. (2006) investigated the scale height of
206 the F region peak using an ionogram. They showed that the F10.7 index shows an increasing
207 trend with an increase of scale height around the F region peak height. At the solar minimum, the
208 altitude extent of the F region peak becomes smaller than during the solar moderate periods
209 because the scale height becomes smaller. Statistically, the most observed period for
210 postmidnight BPDs is low solar activity and June solstice, where F region is known to contract
211 most significantly. Under such conditions, the ionospheric density changes significantly, even for
212 slight altitude changes. As such, low solar activity and June period make a good environment for
213 postmidnight BPDs to occur.

214 For both mechanisms suggested for BPD generation, the uplift of the ionosphere and a
215 merger of bubbles, updraft of the ionosphere should generate favorable conditions for BPD
216 occurrence. In general, the vertical motion of the background plasma is upward during the
217 daytime and downward during the nighttime. The upward drift peaks at about 18LT by
218 prereversal enhancement, and the downward drift has a maximum at about 21LT. The amplitude
219 of the vertical drift varies with the season, and the amplitude also varies with the solar flux (Fejer
220 et al., 1991; 1995). While the amplitude of the vertical drift increases as the solar flux increases,
221 in a low solar flux the amplitude of the vertical drift is small. In lower solar activity, the
222 amplitude of average vertical plasma drifts measured at Jicamarca is very weak (Fejer et al.,
223 1991). Particularly after midnight in the June solstice during low solar activity, background
224 plasma drift is almost stagnant. Figure 5 shows vertical plasma drifts measured by incoherent
225 scatter radar at JRO during three seasons for solar minimum (2008-2009) and solar moderate

226 (2011-2012) periods. During the solar minimum, the ionospheric plasma in June solstice has an
227 upward motion after midnight, unlike other seasons. In the solar moderate period, plasma in all
228 seasons did not drift upward after midnight, but an upward drift appeared in December solstice
229 and equinox around 19 LT. In Figure 3, postmidnight BPDs are frequently observed during June
230 solstice in 2008-2009, while the premidnight BPDs in 2011-2012 occur in December solstice and
231 equinox: the BPD occurrence generally follows the season and solar activity dependence of the
232 vertical drift of the background plasma. The background upward motion, which depends on
233 season and solar activity, is an important factor in BPD generation.

234 The vertical plasma drift measured by C/NOFS Coupled Ion-Neutral Dynamics
235 Investigation (CINDI) also showed that the vertical drift of the background plasma is weakly
236 downward at midnight during low solar activity, but plasma depletion at sunset is rising slowly,
237 so bubbles are observed at midnight (Smith et al., 2018). In addition, Stoneback et al. (2011)
238 reported that the average vertical drifts are mostly downward in May, June, July, and August
239 between 17:00 and 20:00 LT. As the vertical plasma drift is relatively less downward at
240 postmidnight of June solstice during solar minimum, there is more opportunity for the satellite to
241 observe the BPDs.

242 Let us assume a disturbance-induced electric field of the same magnitude at the solar
243 minimum and solar maximum. As the electric field uplifts the equatorial F region, ionospheric
244 density at a fixed altitude changes more rapidly at the solar minimum than at the solar maximum.
245 Two factors are known to change the electric field in the equatorial ionosphere by geomagnetic
246 disturbance. The first is the penetration electric field generated by the sudden changes in the
247 solar wind and magnetosphere, which is generally short-lived (for a few hours at most). The
248 other is the disturbance dynamo electric field caused by the neutral wind, the effect of which can

249 last longer than several hours. Blanc & Richmond (1980) presented a theory called disturbance
250 dynamo. According to this theory, during a magnetic storm, energy is deposited into both polar
251 regions and Joule heating occurs. The concomitant changes in the global wind circulation can
252 induce a westward electric field in dayside and an eastward electric field in the nightside. After
253 midnight, which is the focus of this study, the eastward electric field is induced in the equatorial
254 ionosphere by the effect of disturbance dynamo electric field during the magnetic storm, and the
255 ionosphere plasma is lifted.

256 In June solstice during low solar activity the F region has a small scale height and near-
257 stagnant vertical drifts, which provides a good environment for the growth of BPDs. Under these
258 conditions, the plasma density can change suddenly even at a slight altitude variation because the
259 altitude slope of the plasma density becomes steep. On top of this pre-conditioning the
260 disturbance-induced electric field in the background can lift up the ionosphere, leading to post-
261 midnight BPDs in June at very low solar activity.

262 The bubble distribution was investigated by C/NOFS during solar minimum, and the bubble
263 was seen after midnight in northern summer (Huang et al., 2014). In Figure 6, BPD is well
264 observed at longitude of 0 degree-90 degrees, and according to Huang et al. (2014), bubbles are
265 observed in similar regions. The longitudinal distribution of the BPD is consistent with the
266 distribution of longitude of relative density perturbations as well as plasma density perturbations.
267 However, the number of BPD encounters has a secondary peak in 240 degrees-360 degrees and a
268 minimum in 90 degrees-240 degrees. However, the bubble does not follow the longitudinal
269 distribution of BPDs. That is, the bubble does not show the secondary peak and minimum
270 longitudes. Ionospheric uplift can be favorable to the generation of both bubbles and BPDs,
271 which may be responsible for their common occurrence peaks at longitude of 0 degree-90

272 degrees. However, the longitudinal distributions of BPD and bubble do not completely match, so
273 the mechanism of BPD generation cannot be solely explained by the merging process suggested
274 by Huang et al. (2011).

275 Recently, plasma bubbles have been reported over a wide latitude range in the ionosphere –
276 for example, super plasma bubbles. With storm and concomitant prompt penetration electric field,
277 plasma bubbles occurred in westward Africa and extended to European middle latitude (30°-
278 40°N) (Cherniak et al., 2016). Analysis of Millstone Incoherent scatter radar and GNSS TEC
279 data for geomagnetic storms showed that a strong equatorial plasma bubble was grown and
280 combined with mesoscale traveling ionospheric disturbances (Aa et al., 2019). These super
281 plasma bubbles seemed to span a wide latitude range, just as equatorial BPDs have a large
282 longitudinal extent. The relationship between BPDs and super plasma bubbles is an interesting
283 topic, which has been left for future study.

284

285 **4.2. Premidnight BPDs during moderate solar activity**

286 Although the occurrence rate is low, premidnight BPDs occur mainly during relatively high
287 solar activity. During this period, the equatorial ionosphere does not necessarily have a lower
288 scale height and weakly downward plasma drift: it is not a good environment for the occurrence
289 of BPDs. Premidnight BPDs are observed with high Kp indices, which signifies strong storms. If
290 an exceptionally strong eastward electric field is induced in the pre-midnight equatorial
291 ionosphere by the prompt penetration electric field effect, the F region uplift can become
292 stronger even though the background electric field is directed westward. The requirement for
293 exceptional strength of eastward E-field may explain the low occurrence of pre-midnight BPDs
294 during relatively higher solar activity in comparison to that of post-midnight BPDs during solar

295 minimum years. Considering the statistical properties of the two groups of BPDs divided by
296 local time, the BPDs occurrences depend strongly on local time and solar activity. When the
297 lower scale height and stagnant background make favorable environments for BPD generation
298 during solar minimum, the storm-time disturbance dynamo can easily trigger the uplift of the
299 equatorial ionosphere and generate prominent BPDs. It was considered as BPDs when satellite
300 pass through the larger structure of plasma density depletion.

301

302 **5. Conclusions**

303 We have investigated the statistical distribution in the occurrence of BPDs using the plasma
304 density data measured by the PLP instrument on board the C/NOFS satellite in 2008-2012. We
305 have also developed a code to find BPDs automatically.

306 Although premidnight BPDs have been found in previous studies, BPDs are mainly
307 observed at lower apex height at postmidnight. BPDs were also frequently observed in the June
308 solstice of low solar activity. The tendency of the BPD occurrence rate was similar to that of the
309 AE index, and showed a clear inverse correlation with the 10.7 cm solar radio flux.

310 Why are BPDs often observed in postmidnight, solar minimum, and June solstice? The
311 reason why BPD is frequently observed in low solar activity periods is because lower scale
312 height and stagnant post-midnight background plasma forms a favorable environment for the
313 production of BPDs. Under this pre-condition, storm-time disturbance dynamo can easily
314 generate post-midnight BPDs. Even if the F region rises slightly due to the disturbance-induced
315 electric field, the satellites can pass through the bottomside plasma more easily than for high
316 solar activity.

317 Since the F region is thick in high solar activity, a strong disturbance-induced electric field
318 in support of eastward background field (e.g., pre-reversal enhancement) is necessary in order for
319 the F region to be raised to create the BPD at satellite altitudes. Therefore, we suggest that BPDs
320 in high solar activity are observed only if a strong prompt penetration electric field is superposed
321 to pre-reversal enhancement in premidnight. A satellite at lower apex altitudes has a higher
322 chance of detecting BPD.

323
324
325

326 **Acknowledgements**

327 This research was supported by basic research funding from Korea Astronomy and Space
328 Science Institute (KASI). J.-M. Choi was also supported by the Ministry of Science and
329 Technology, Taiwan (MOST) under project MOST 108-2638-M-006-001-MY2. Part of the work
330 is supported by National Space Organization, Taiwan (NSPO) under project NSPO-S-109065.
331 The C/NOFS data are available in the NASA database (http://cdaweb.gsfc.nasa.gov/istp_public/).
332 The Jicamarca ISR data for this paper were obtained from the CEDAR Madrigal Database at
333 <http://cedar.openmadrigal.org>. The OMNI data were obtained from the GSFC/SPDF OMNIWeb
334 interface at <https://omniweb.gsfc.nasa.gov>.

335 **References**

336

337 Aa, E., Zou, S., Ridley, A. J., Zhang, S.-R., Coster, A. J., Erickson, P. J., et al. (2019). Merging
338 of storm time mid-latitude traveling ionospheric disturbances and equatorial plasma bubbles.
339 *Space Weather*, 17, 285– 298. <https://doi.org/10.1029/2018SW002101>

340

341 Abdu, M. A., Bittencourt, J. A., & Batista, I. S. (1981). Magnetic declination control of the
342 equatorial *F* region dynamo electric field development and spread *F*. *Journal of Geophysical*
343 *Research*, 86, 11,443–11,446. <https://doi.org/10.1029/JA086iA13p11443>

344

345 Abdu, M. A., Batista, I. S., & Sobral, J. (1992). A new aspect of magnetic declination control of
346 equatorial spread *F* and *F* region dynamo. *Journal of Geophysical Research*, 97(A10), 14,897–
347 14,904. <https://doi.org/10.1029/92JA00826>

348

349 Abdu, M. A., Kherani, E. A., Batista, I. S., & Sobral, J. H. A. (2009). Equatorial evening
350 prereversal vertical drift and spread *F* suppression by disturbance penetration electric fields.
351 *Geophysical Research Letter*, 36, L19103. <https://doi.org/10.1029/2009GL039919>

352

353 Basu, S., Basu, S., Rich, F. J., Groves, K. M., MacKenzie, E., Coker, C., Sahai, Y., Fagundes, P.
354 R., & Becker-Guedes, F. (2007). Response of the equatorial ionosphere at dusk to penetration
355 electric fields during intense magnetic storms. *Journal of Geophysical Research*, 112, A08308.
356 <https://doi.org/10.1029/2006JA012192>

357

358 Blanc, M., & Richmond, A. (1980). The ionospheric disturbance dynamo. *Journal of*
359 *Geophysical Research*, *85(A4)*, 1669– 1686. <https://doi.org/10.1029/JA085iA04p01669>
360

361 Burke, W. J., Rubin, A. G., Maynard, N. C., Gentile, L. C., Sultan, P. J., Rich, F. J., de La
362 Beaujardière, O., Huang, C. Y., & Wilson, G. R. (2000). Ionospheric disturbances observed by
363 DMSP at middle to low latitudes during the magnetic storm of June 4–6, 1991. *Journal of*
364 *Geophysical Research*, *105(A8)*, 18,391–18,405. <https://doi.org/10.1029/1999JA000188>
365

366 Burke, W. J., de La Beaujardière, O., Gentile, L. C., Hunton, D. E., Pfaff, R. F., Roddy, P. A.,
367 Su, Y.-J., & Wilson, G. R. (2009). C/NOFS observations of plasma density and electric field
368 irregularities at post-midnight local times. *Geophysical Research Letter*, *36*, L00C09.
369 <https://doi.org/10.1029/2009GL038879>
370

371 Cherniak, I., & Zakharenkova, I. (2016). First observations of super plasma bubbles in Europe.
372 *Geophysical Research Letter*, *43*, 11,137– 11,145. <https://doi.org/10.1002/2016GL071421>
373

374 Fejer, B. G., dePaula, E. R., Gonzalez, S. A., & Woodman, R. F. (1991). Average vertical and
375 zonal F region plasma drifts over Jicamarca. *Journal of Geophysical Research*, *96(A8)*, 13,901–
376 13,906. <https://doi.org/10.1029/91JA01171>
377

378 Fejer, B. G., dePaula, E. R., Heelis, R. A., & Hanson, W. B. (1995). Global equatorial
379 ionospheric vertical plasma drifts measured by the AE-E satellite. *Journal of Geophysical*
380 *Research*, *100*, 5769–5776. <https://doi.org/10.1029/94JA03240>

381

382 Greenspan, M. E., Rasmussen, C. E., Burke, W. J., & Abdu, M. A. (1991). Equatorial density
383 depletions observed at 840 km during the greatmagnetic storm of March 1989. *Journal of*
384 *Geophysical Research*, 96(A8), 13,931–13,942. <https://doi.org/10.1029/91JA01264>

385

386 Hargreaves, J. K. (1992). *The Solar-Terrestrial Environment*, 218 pp., Cambridge Univ. Press,
387 Cambridge, U. K.

388

389 Huang, C.-S., de La Beaujardière, O., Roddy, P. A., Hunton, D. E., Pfaff, R. F., Valladares, C.
390 E., & Ballenthin, J. O. (2011). Evolution of equatorial ionospheric plasma bubbles and formation
391 of BPDs measured by the C/NOFS satellite during deep solar minimum. *Journal of Geophysical*
392 *Research*, 116, A03309. <https://doi.org/10.1029/2010JA015982>

393

394 Huang, C.-S., Retterer, J. M., de La Beaujardière, O., Roddy, P. A., Hunton, D. E., Ballenthin, J.
395 O., & Pfaff, R. F. (2012). Observations and simulations of formation of broad plasma depletions
396 through merging process. *Journal of Geophysical Research*, 117, A02314.
397 <https://doi.org/10.1029/2011JA017084>

398

399 Huang, C.-S., La Beaujardiere, O., Roddy, P. A., Hunton, D. E., Liu, J. Y., and Chen, S. P.
400 (2014). Occurrence probability and amplitude of equatorial ionospheric irregularities associated
401 with plasma bubbles during low and moderate solar activities (2008–2012). *Journal of*
402 *Geophysical Research: Space Physics*, 119, 1186– 1199. <https://doi.org/10.1002/2013JA019212>

403

404 Huang, C. Y., Marcos, F. A., Roddy, P. A., Hairston, M. R., Coley, W. R., Roth, C., Bruinsma,
405 S., and Hunton, D. E. (2009). Broad plasma decreases in the equatorial ionosphere. *Geophysical*
406 *Research Letter*, *36*, L00C04. <https://doi.org/10.1029/2009GL039423>
407

408 Kil, H., & Paxton, L. J. (2006). Ionospheric disturbances during the magnetic storm of 15 July
409 2000: Role of the fountain effect and plasma bubbles for the formation of large equatorial plasma
410 density depletions. *Journal of Geophysical Research*, *111*, A12311.
411 <https://doi.org/10.1029/2006JA011742>
412

413 Kil, H., Paxton, L. J., Su, S.-Y., Zhang, Y., & Yeh, H. (2006). Characteristics of the storm-
414 induced big bubbles (SIBBs). *Journal of Geophysical Research*, *111*, A10308.
415 <https://doi.org/10.1029/2006JA011743>
416

417 Kil, H., & Lee, W. K. (2013). Are plasma bubbles a prerequisite for the formation of broad
418 plasma depletions in the equatorial F region?. *Geophysical Research Letter*, *40*, 3491–3495.
419 <https://doi.org/10.1002/grl.50693>
420

421 Kil, H., Kwak, Y.-S., Lee, W. K., Oh, S.-J., Milla, M., & Galkin, I. (2014). Broad plasma
422 depletions detected in the bottomside of the equatorial F region: Simultaneous ROCSAT-1 and
423 JULIA observations, *Journal of Geophysical Research: Space Physics*, *119*, 5978–5984.
424 <https://doi.org/10.1002/2014JA019964>
425

426 Kil, H., Lee, W. K., Paxton, L. J., Hairston, M. R., & Jee, G. (2016). Equatorial broad plasma
427 depletions associated with the evening prereversal enhancement and plasma bubbles during the
428 17 March 2015 storm. *Journal of Geophysical Research: Space Physics*, *121*, 10,209–10,219.
429 <https://doi.org/10.1002/2016JA023335>

430

431 Lee, J. J., Min, K. W., Kim, V. P., Hegai, V. V., Oyama, K.-I., Rich, F. J., & Kim, J. (2002).
432 Large density depletions in the nighttime upper ionosphere during the magnetic storm of July 15,
433 2000. *Geophysical Research Letter*, *29*(3), 1032. <https://doi.org/10.1029/2001GL013991>

434

435 Lee, W. K., Kil, H., Kwak, Y.-S., Paxton, L. J., Zhang, Y., Galkin, I., & Batista, I. S. (2014).
436 Equatorial broad plasma depletions associated with the enhanced fountain effect. *Journal of*
437 *Geophysical Research*, *119*, 402–410. <https://doi.org/10.1002/2013JA019137>

438

439 Lee, C.-C., & Reinisch, B. W. (2007). Quiet-condition variations in the scale height at F2-layer
440 peak at Jicamarca during solar minimum and maximum. *Annales Geophysicae*, *25*(12), 2541–
441 2550. <https://doi.org/10.5194/angeo-25-2541-2007>

442

443 Liu, L., Wan, W., & Ning, B. (2006). A study of the ionogram derived effective scale height
444 around the ionospheric hmF₂. *Annales Geophysicae*, *24*(3), 851–860.
445 <https://doi.org/10.5194/angeo-24-851-2006>

446

447 Liu, L., Yang, J., Le, H., Chen, Y., Wan, W., & Lee, C.-C. (2012). Comparative study of the
448 equatorial ionosphere over Jicamarca during recent two solar minima. *Journal of Geophysical*
449 *Research*, *117*, A01315, <https://doi.org/10.1029/2011JA017215>
450

451 Nishioka, M., Otsuka, Y., Shiokawa, K., Tsugawa, T., Effendy, Supnithi, P., Nagatsuma, T., &
452 Murata, K. T. (2012). On post-midnight field-aligned irregularities observed with a 30.8-MHz
453 radar at a low latitude: Comparison with F-layer altitude near the geomagnetic equator. *Journal*
454 *of Geophysical Research*, *117*, A08337, <https://doi.org/10.1029/2012JA017692>
455

456 Su, S.-Y., Yeh, H. C., Chao, C. K., & Heelis, R. A. (2002). Observation of a large density
457 dropout across the magnetic field at 600 km altitude during the 6–7 April 2000 magnetic storm.
458 *Journal of Geophysical Research*, *107*(A11), 1404, <https://doi.org/10.1029/2001JA007552>
459

460 Smith, J. M., & Heelis, R. A. (2018). The plasma environment associated with equatorial
461 ionospheric irregularities. *Journal of Geophysical Research: Space Physics*, *123*, 1583– 1592.
462 <https://doi.org/10.1002/2017JA024933>
463

464 Stoneback, R. A., Heelis, R. A., Burrell, A. G., Coley, W. R., Fejer, B. G., & Pacheco, E. (2011).
465 Observations of quiet time vertical ion drift in the equatorial ionosphere during the solar
466 minimum period of 2009. *Journal of Geophysical Research*, *116*, A12327.
467 <https://doi.org/10.1029/2011JA016712>
468

469 Yokoyama, T., Shinagawa, H., & Jin, H. (2014). Nonlinear growth, bifurcation and pinching of
470 equatorial plasma bubble simulated by three-dimensional high-resolution bubble model. *Journal*
471 *of Geophysical Research: Space Physics*, *119*, 10,474–10,482.
472 <https://doi.org/10.1002/2014JA020708>

473

474

475

476

477

478

479

480

481

482

483

484

485

486

487

488

489

490

491

492 **Figure captions**

493 **Figure 1.** Examples of automatic BPDs search process in the C/NOFS satellite data. (a) In-situ
494 measurements of plasma density. The red solid line represents the background density. (b) The
495 difference between the logarithm of the plasma density and logarithm of the background density.
496 (c) The absolute values of the results in Figure 1b. The red dashed line represents the threshold
497 value. (d) Results considered the threshold value. (e) The final processed BPDs.

498

499 **Figure 2.** Statistical distribution of the occurrence of BPDs as a function of (a) local time, (b)
500 magnetic latitude, (c) the Kp index, and (d) apex altitude, when BPDs were automatically
501 searched in the C/NOFS data from June 2008 to December 2012. Blue and green bars indicate
502 the occurrence rates of the postmidnight PBDs and the premidnight BPDs, respectively.

503

504 **Figure 3.** Monthly distribution of occurrence rate of BPDs observed by C/NOFS satellite during
505 2008-2012. The blue lines show the AE index.

506

507 **Figure 4.** Seasonal variation of BPDs in (a) June solstice, (b) December solstice, (c) equinox.
508 The red lines indicate the 10.7 cm solar radio flux.

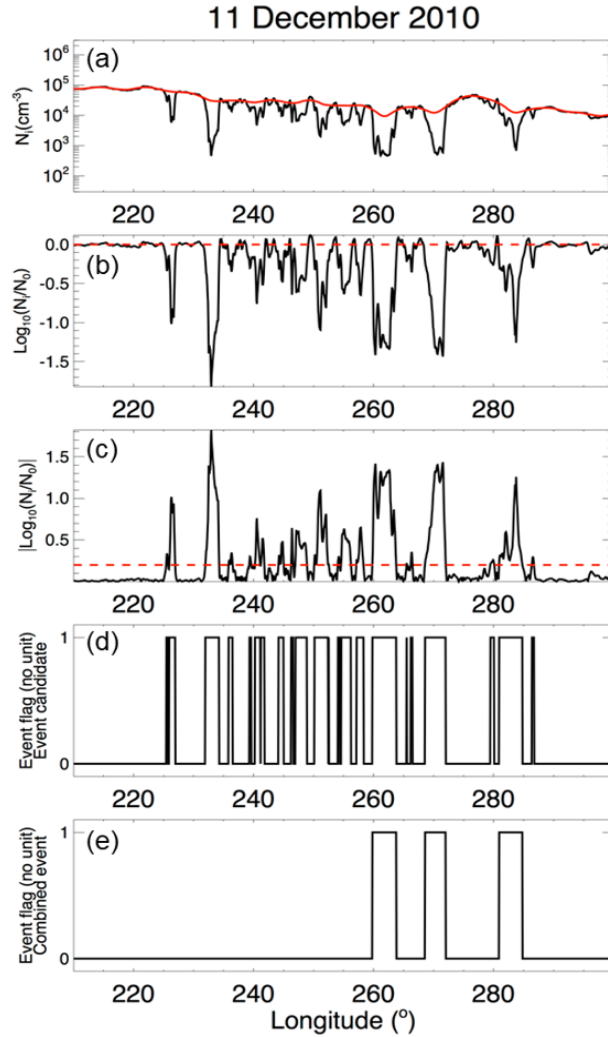
509

510 **Figure 5.** Median vertical plasma drifts over Jicamarca during June solstice (May, June, July,
511 and August), December solstice (November, December, January, and February), and equinox
512 (March, April, September, and October) for solar minimum and moderate flux conditions. The
513 error bars denote upper and lower quartile of the median values. The left and right panel indicate
514 median vertical plasma drift in solar minimum (2008-2009) and solar moderate (2011-2012),
515 respectively. The number of data points is given at the top of each panel.

516

517 **Figure 6.** Longitudinal variation of BPDs.

518



519

520 **Figure 1.** Examples of automatic BPDs search process in the C/NOFS satellite data. (a) In-situ
 521 measurements of plasma density. The red solid line represents the background density. (b) The
 522 difference between the logarithm of the plasma density and logarithm of the background density.
 523 (c) The absolute values of the results in Figure 1b. The red dashed line represents the threshold
 524 value. (d) Results considered the threshold value. (e) The final processed BPDs.

525

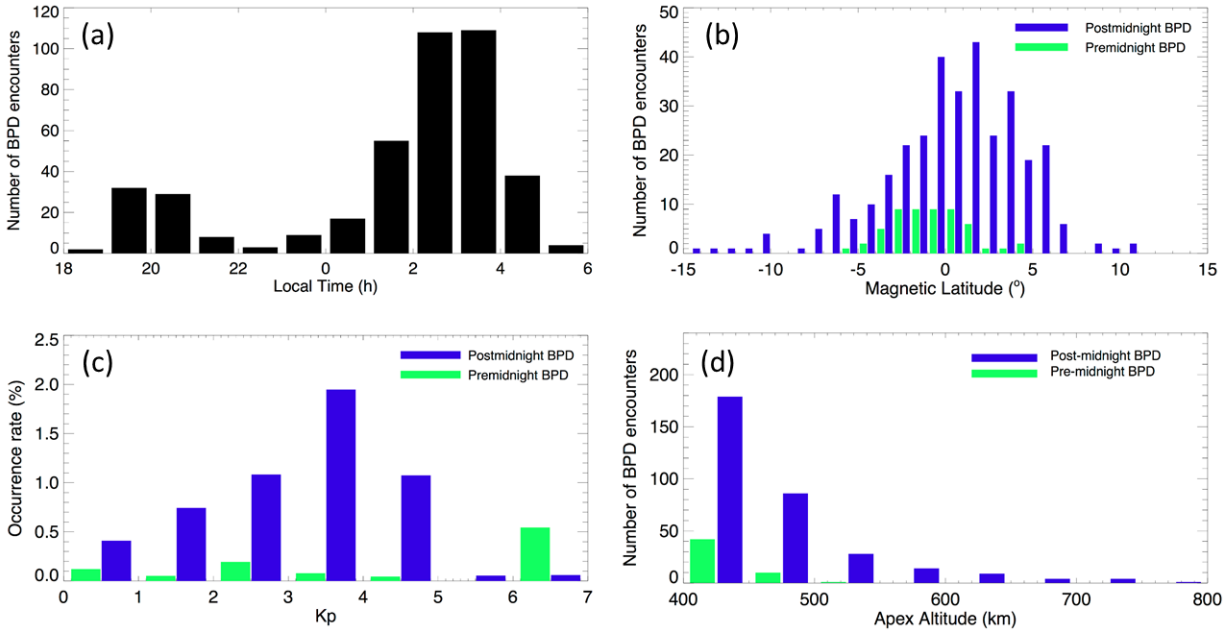
526

527

528

529

530



531

532 **Figure 2.** Statistical distribution of the occurrence of BPDs as a function of (a) local time, (b)
 533 magnetic latitude, (c) the Kp index, and (d) apex altitude, when BPDs were automatically
 534 searched in the C/NOFS data from June 2008 to December 2012. Blue and green bars indicate
 535 the occurrence rates of the postmidnight PBDs and the premidnight BPDs, respectively.

536

537

538

539

540

541

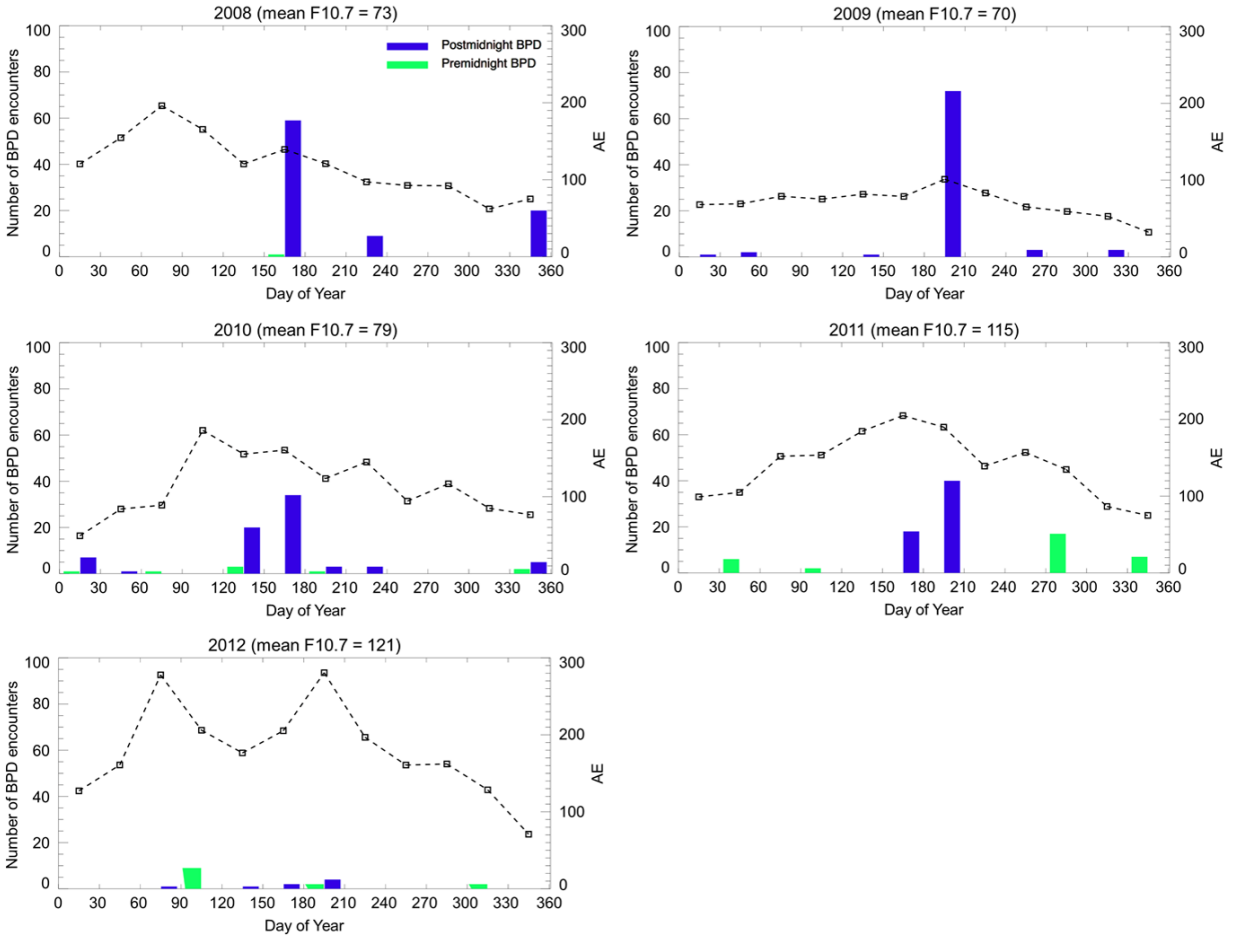
542

543

544

545

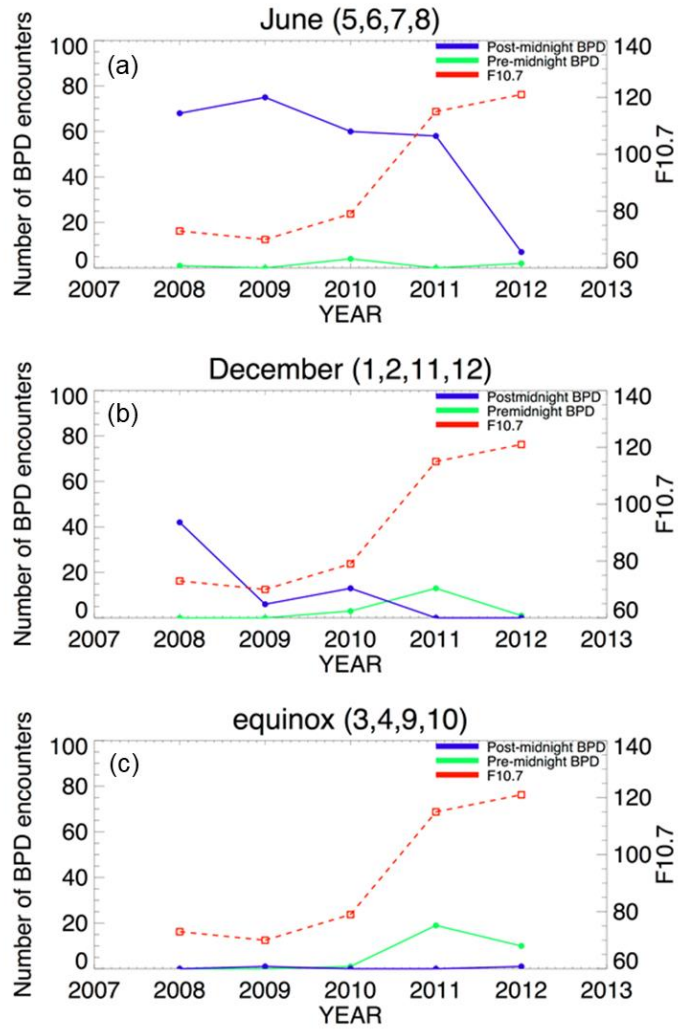
546



547

548 **Figure 3.** Monthly distribution of occurrence rate of BPDs observed by C/NOFS satellite during
 549 2008-2012. The black dashed lines show the AE index.

550



551

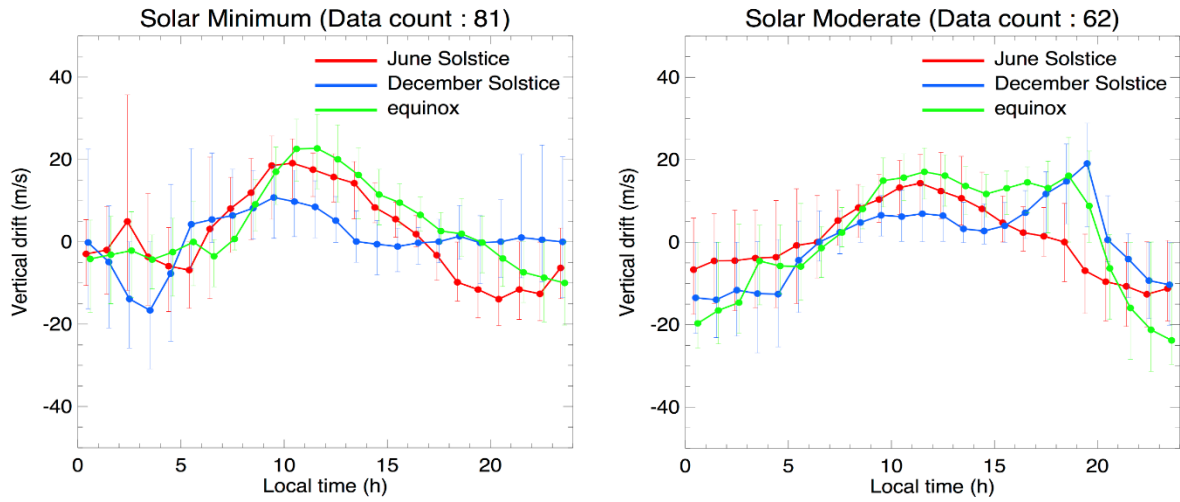
552 **Figure 4.** Year-to-year variation of BPDs in (a) June solstice, (b) December solstice, (c) equinox.
 553 The red dashed lines indicate the 10.7 cm solar radio flux.

554

555

556

557



558

559 **Figure 5.** Median vertical plasma drifts over Jicamarca during June solstice (May, June, July,
 560 and August), December solstice (November, December, January, and February), and equinox
 561 (March, April, September, and October) for solar minimum and moderate flux conditions. The
 562 error bars denote upper and lower quartile of the median values. The left and right panel indicate
 563 median vertical plasma drift in solar minimum (2008-2009) and solar moderate (2011-2012),
 564 respectively. The number of data points is given at the top of each panel.

565

566

567

568

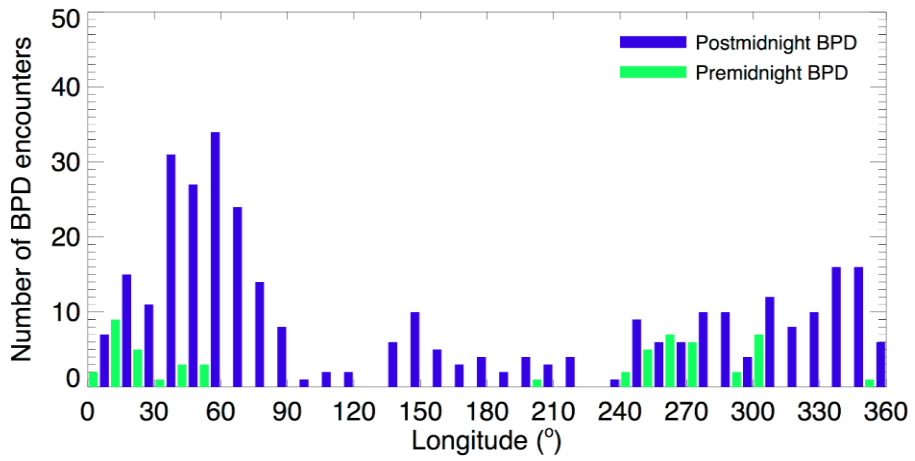
569

570

571

572

573



574

575 **Figure 6.** Longitudinal variation of BPDs.

576

577

578

579

580

581

582

Figure 1.

11 December 2010

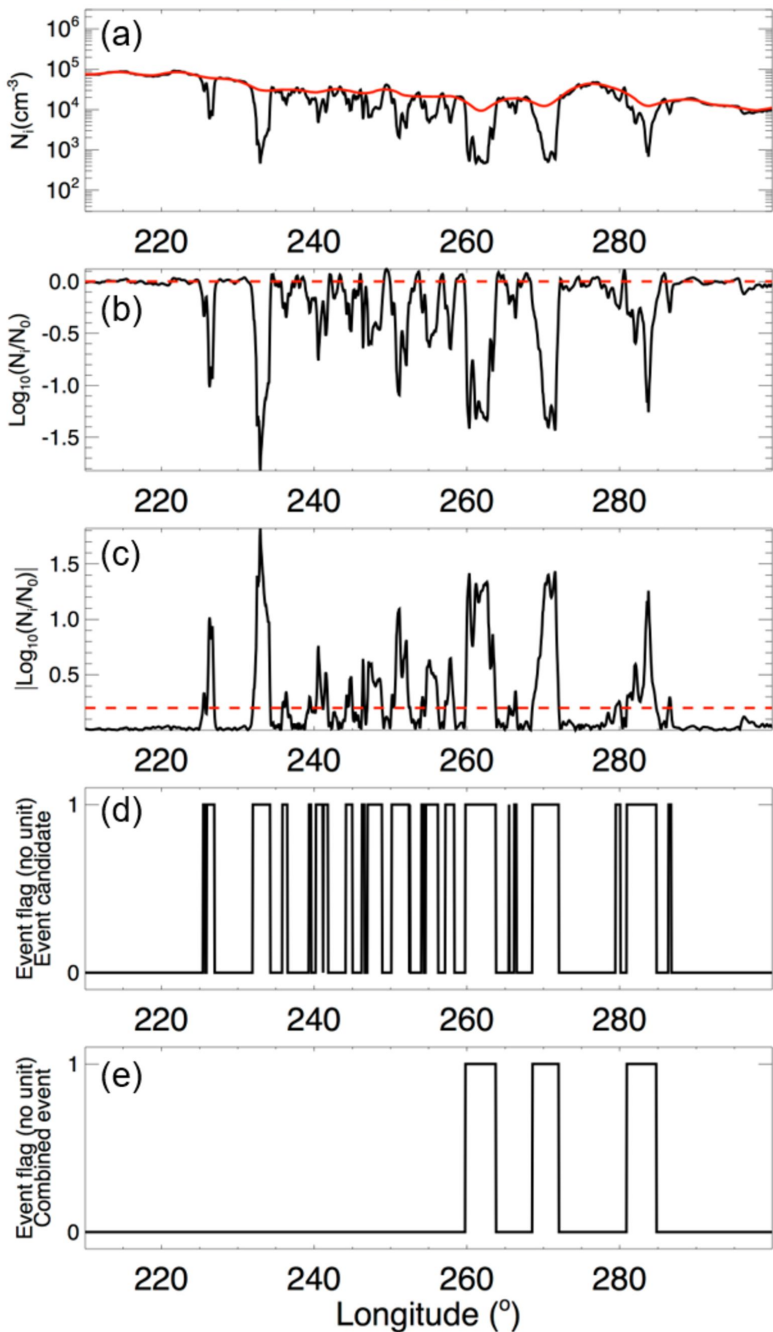


Figure 2.

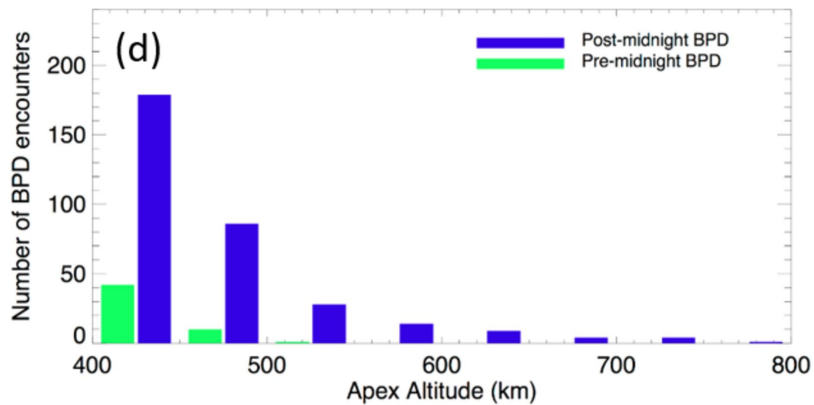
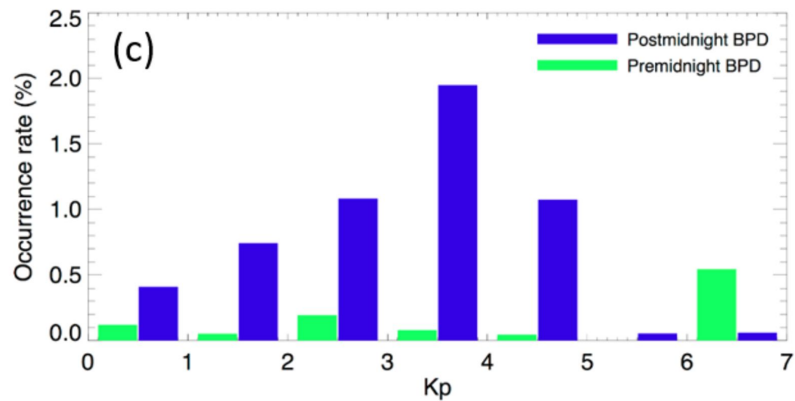
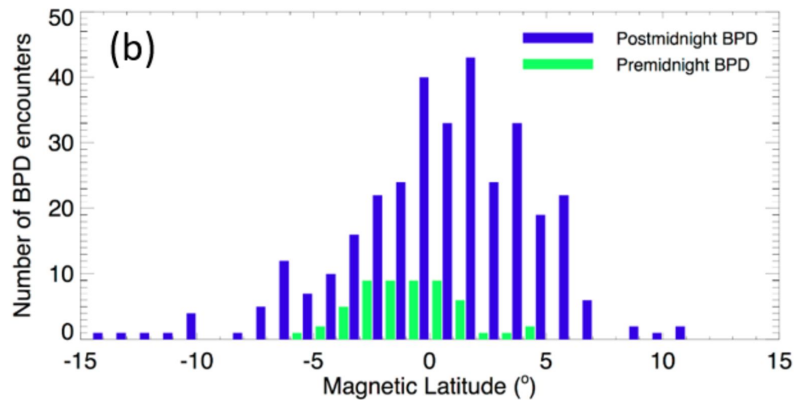
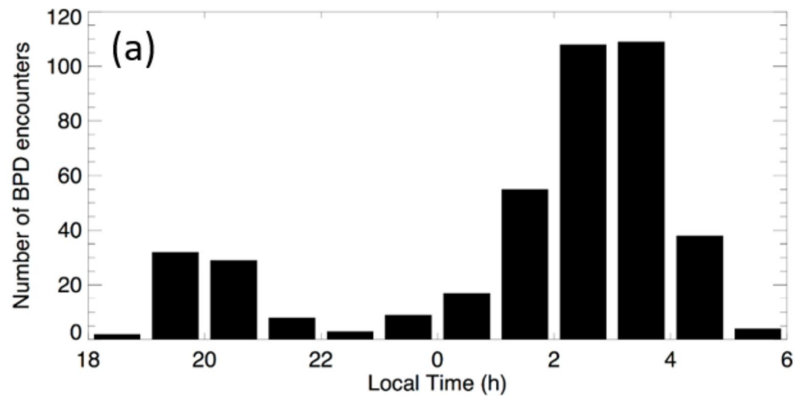
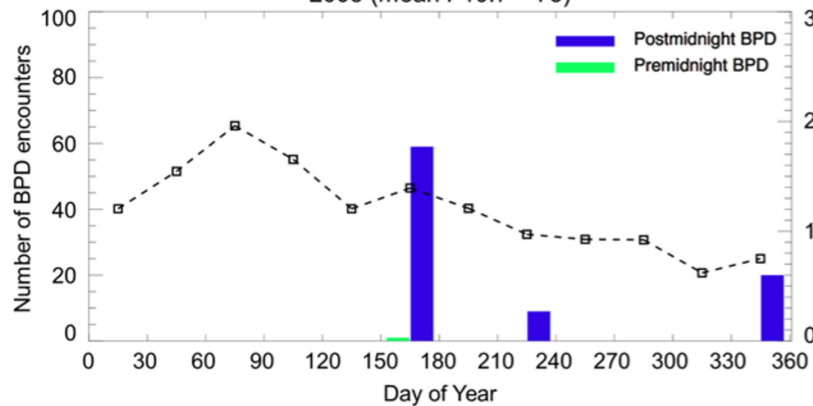
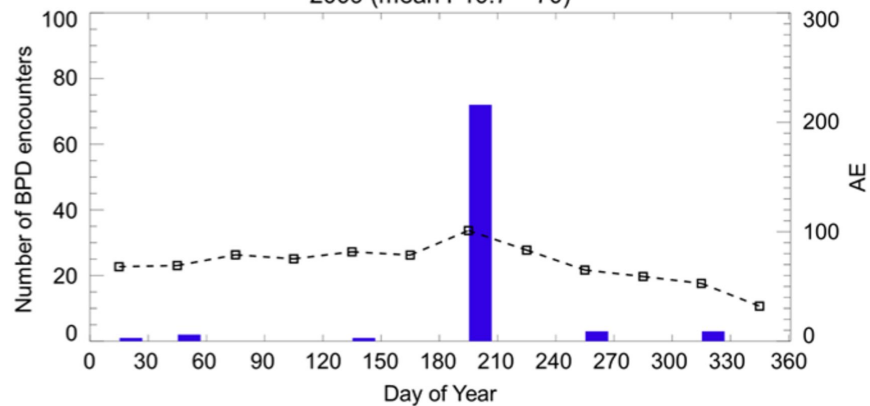


Figure 3.

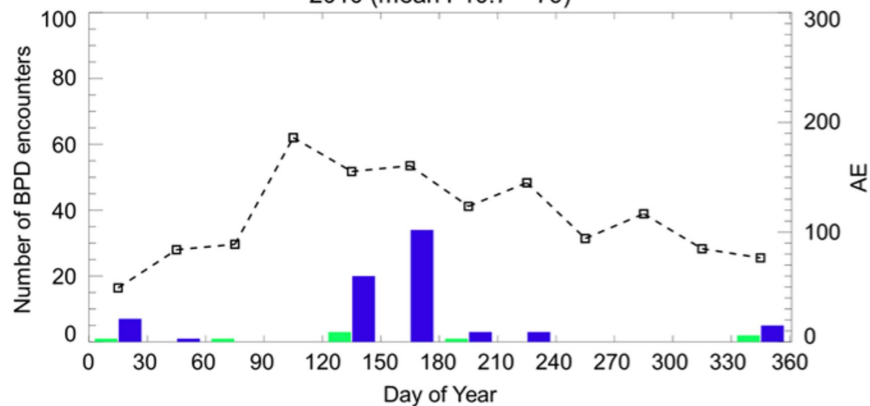
2008 (mean F10.7 = 73)



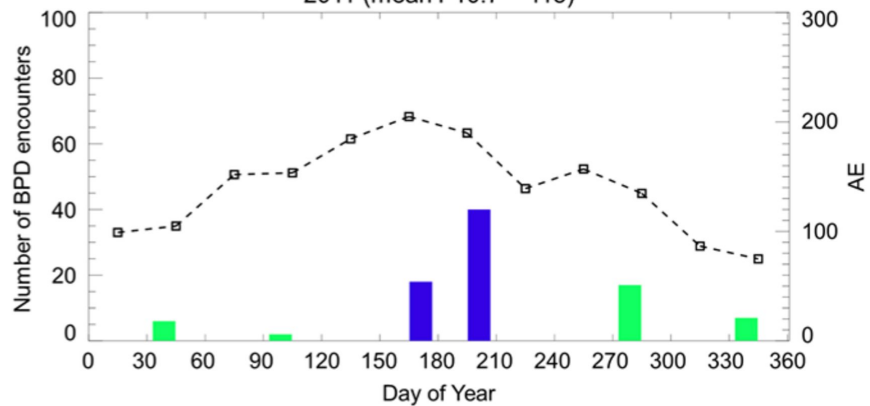
2009 (mean F10.7 = 70)



2010 (mean F10.7 = 79)



2011 (mean F10.7 = 115)



2012 (mean F10.7 = 121)

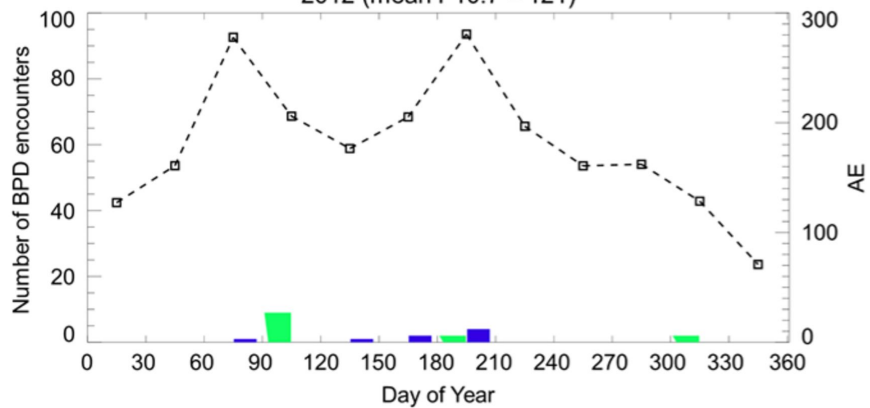


Figure 4.

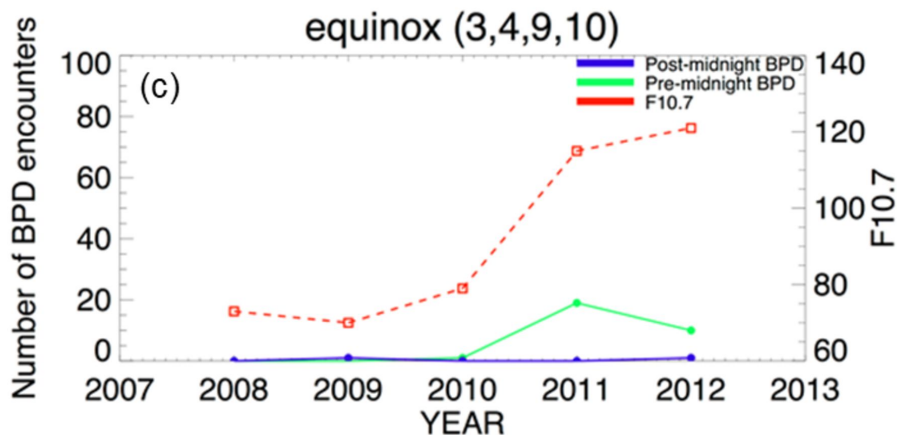
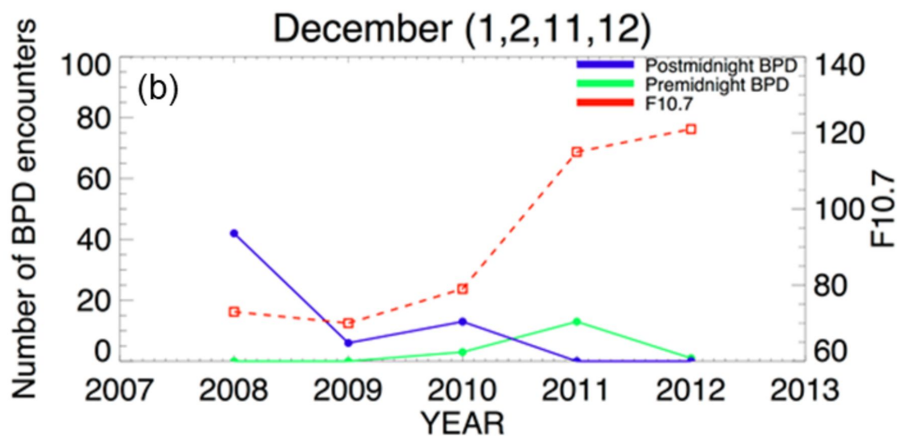
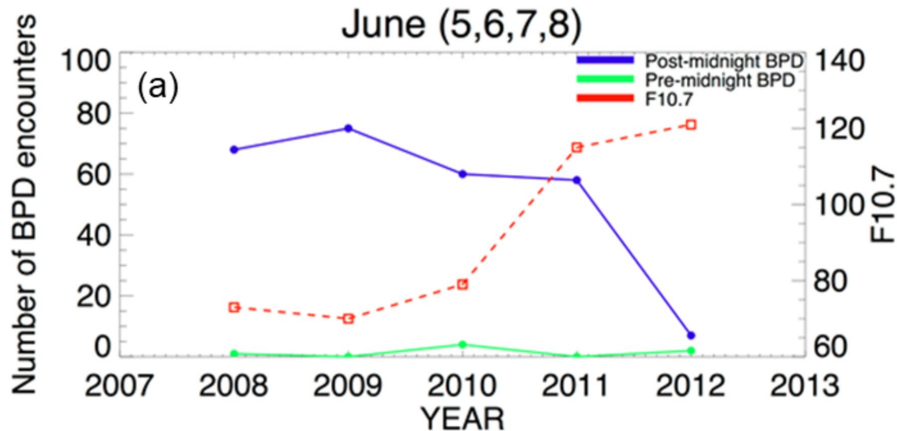
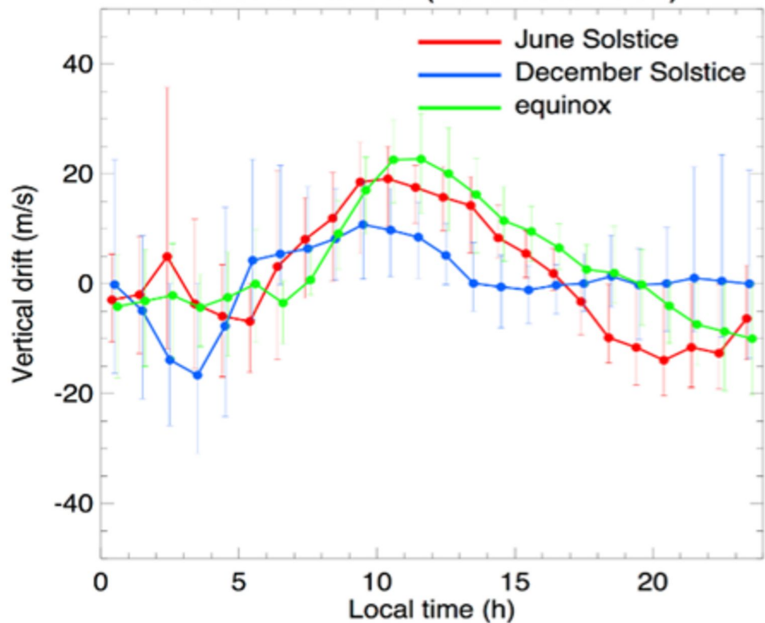


Figure 5.

Solar Minimum (Data count : 81)



Solar Moderate (Data count : 62)

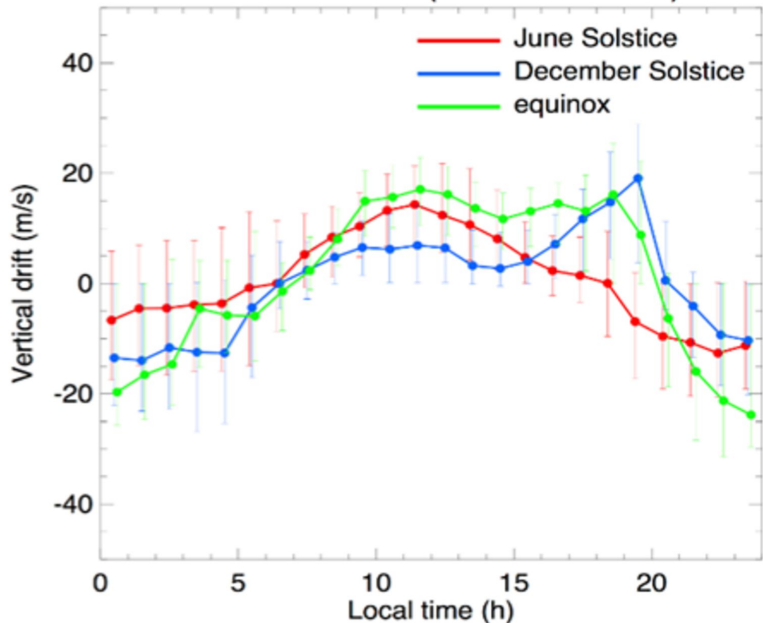


Figure 6.

